



OPEN

SUBJECT AREAS:

MATERIALS SCIENCE

APPLIED PHYSICS

BATTERIES

CARBON NANOTUBES AND  
FULLERENES

# Rechargeable Batteries with High Energy Storage Activated by In-situ Induced Fluorination of Carbon Nanotube Cathode

Xinwei Cui<sup>1</sup>, Jian Chen<sup>2</sup>, Tianfei Wang<sup>1</sup> & Weixing Chen<sup>1,3</sup>

<sup>1</sup>AdvEn Solutions Inc., 3231 Tredger Close, Edmonton, Alberta, Canada, T6R 3T6, <sup>2</sup>National Institute for Nanotechnology, NINT, NRC, 11421 Saskatchewan Drive, Edmonton, Alberta, Canada, T6G 2M9, <sup>3</sup>Department of Chemical and Materials Engineering, University of Alberta, Edmonton, Alberta, Canada T6G 2G6.

Received  
31 March 2014Accepted  
29 May 2014Published  
16 June 2014

Correspondence and requests for materials should be addressed to X.W.C. (xinwei.cui@adven-solutions.com) or W.X.C. (weixing.chen@ualberta.ca)

High performance rechargeable batteries are urgently demanded for future energy storage systems. Here, we adopted a lithium-carbon battery configuration. Instead of using carbon materials as the surface provider for lithium-ion adsorption and desorption, we realized induced fluorination of carbon nanotube array (CNTA) paper cathodes, with the source of fluoride ions from electrolytes, by an in-situ electrochemical induction process. The induced fluorination of CNTA papers activated the reversible fluorination/defluorination reactions and lithium-ion storage/release at the CNTA paper cathodes, resulting in a dual-storage mechanism. The rechargeable battery with this dual-storage mechanism demonstrated a maximum discharging capacity of 2174 mAh g<sub>carbon</sub><sup>-1</sup> and a specific energy of 4113 Wh kg<sub>carbon</sub><sup>-1</sup> with good cycling performance.

Although Li-ion batteries (LIBs) have transformed portable electronics, the energy density and cycle life of existing LIBs, even if fully developed, remain insufficient<sup>1,2</sup>. Reaching beyond the horizon of LIBs requires the exploration of new electrochemistry and/or new materials<sup>1</sup>. The recent popular attempts are Li-sulfur (Li-S)<sup>2-7</sup> and Li-air (Li-O<sub>2</sub>) batteries<sup>8-11</sup>. However, there are some formidable challenges for Li-S and Li-O<sub>2</sub> batteries, e.g., dissolution of discharging products, poor cathode electrical conductivity, and large volume expansion upon lithiation<sup>2,4</sup>.

Li-CF<sub>x</sub> batteries have the highest energy density among all primary lithium batteries<sup>12</sup> with a theoretical specific energy of 2180 Wh kg<sub>(Li+CF)</sub><sup>-1</sup>. A high capacity of 615 mAh g<sub>CF<sub>x</sub></sub><sup>-1</sup> was also reported for the pre-synthesized CF<sub>x</sub> cathodes<sup>13</sup>. It is well known that defluorination of carbon fluorides can be achieved with the assistance of lithium cations during discharging in Li-CF<sub>x</sub> batteries<sup>14,15</sup>. However, Li-CF<sub>x</sub> batteries have attracted limited interest because of their strictly non-rechargeable nature<sup>16</sup> and the non-environmental-friendly synthesis process for carbon fluorides, e.g., the use of F<sub>2</sub> gas and/or catalysts under extreme temperature conditions<sup>12-15,17</sup>.

In a departure from previous approaches, we adopted the lithium-carbon battery configuration. Instead of using carbon materials as the surface provider for lithium-ion adsorption and desorption, we realized induced fluorination of carbon nanotube array (CNTA) paper cathodes, with the source of fluoride ions from electrolytes, by an in-situ electrochemical induction process. The induced fluorination of CNTA papers activates the reversible fluorination/defluorination reactions and lithium-ion storage/release at the CNTA paper cathodes, resulting in a dual-storage mechanism. It is the first time that the reversible fluorination/defluorination reactions were realized at pure carbon and non-fluoride materials. The rechargeable battery with this dual-storage mechanism, as shown in Figure 1, is referred to as lithium-carbon-fluorine (Li-C-F) batteries. The cathode of the Li-C-F batteries in this report is made of CNTA papers (Figure S1 in supplementary materials); and hence, it is also denoted as Li-CNT-F batteries. After the battery cells were assembled, CNTA paper cathodes with no binding materials and no conductive additives were in-situ fluorinated by induction charging for a number of cycles, which enables Li-CNT-F batteries with high energy density and high reversibility.

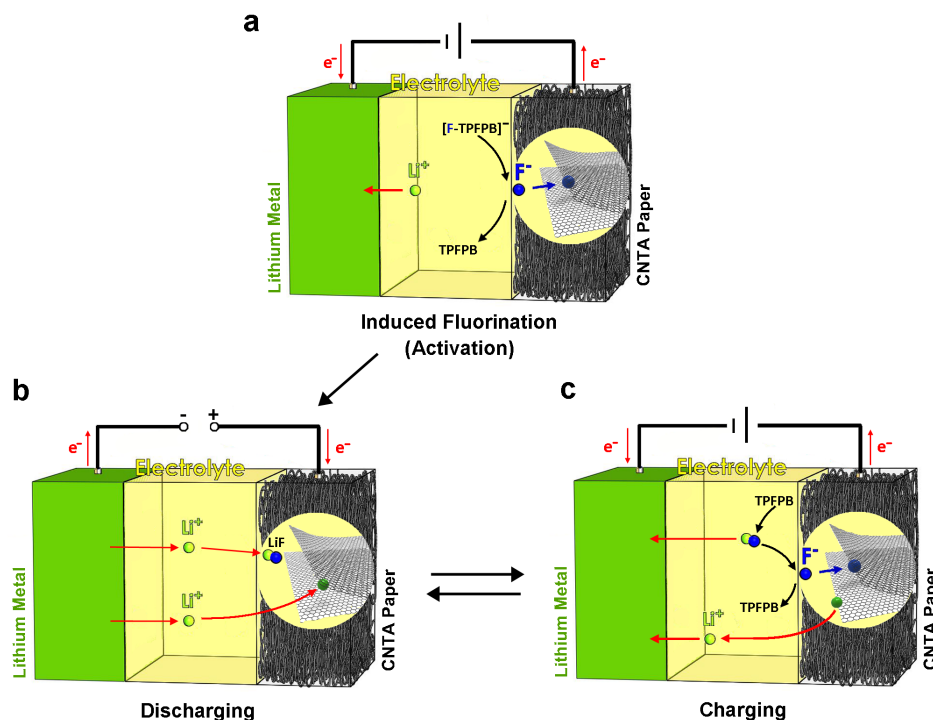


**Figure 1 | Dual-storage mechanism with reversible fluorination/defluorination reactions and lithium-ion storage/release occurring at CNTA paper cathode.** (a) Induced fluorination of CNTA papers occurring at the potential plateau over 4.4 V during an electrochemical induction process at 70°C, which also destroys the graphitic carbon structure to defective structures. (b) Defluorination of the in-situ formed carbon fluorides by the conversion reaction with lithium ions; meanwhile, additional lithium ions store in the defective carbons. (c) Lithium ions release from the defective carbons; meanwhile, the fluorination of the defective carbons by the reversed conversion reaction in (b). In particular, the LiF metastable solids formed in (b) and facing the electrolyte will be dissociated during charging with assistance of TPFPB.

## Results

**In-situ electrochemical induction of carbon nanotube array paper cathodes.** CNTA papers<sup>18</sup> were prepared simply by rolling and pressing 1.2 mm-thick CNT arrays grown on whole silicon wafers (Figure S1). In order to minimize the decomposition of the LiPF<sub>6</sub> organic electrolyte commonly used in LIB at high potentials, an electrolyte comprising of LiF and a fluoride-anion receptor of tris(pentafluorophenyl)borane (TPFPB) in the organic solvents was formulated and demonstrated excellent electrochemical stability over 4.5 V vs. Li/Li<sup>+</sup> at 22°C and 70°C (Figure S2 in supplementary materials). The conductive and binder-free CNTA paper cathodes with a CNT mass loading of 1.4–1.8 mg cm<sup>-2</sup> were then assembled in the aforementioned electrolyte facing lithium metals in 2032-type coin cells.

After the battery cells were assembled, an electrochemical induction process was conducted, during which the induced fluorination of CNTA papers was realized at the charging potential plateau over 4.4 V. Two in-situ electrochemical induction processes are introduced in this report. One process, denoted as Process A1, was performed at 70°C using a controlled charging capacity method. The battery was slowly charged and discharged for two induction cycles, with the charging capacities being controlled at 900 mAh g<sup>-1</sup> for the first cycle and 1400 mAh g<sup>-1</sup> for the second cycle (Figure 2a). The constant current density used was 0.1 A g<sup>-1</sup> and the lower potential limit was set at 1.4 V. The battery shows pure supercapacitive behavior and a low discharging capacity, 102 mAh g<sup>-1</sup>, if the potential is cut off at 4.4 V (the black lines in Figure 2a). When the potential goes higher than 4.4 V at 70°C, a potential plateau at 4.49 V is seen (the green lines in Figure 2a), which corresponds to the induced fluorination of CNTA papers as discussed later. This induced fluorination resulted in a substantial increase in the discharging capacity (764 mAh g<sup>-1</sup>), indicating an activation effect by the induced fluorination. No potential plateau has been observed if the induction

process was performed at lower temperatures, revealing the importance of the induction temperature (Figure S3 in supplementary materials). During the second induction cycle, the potential plateau retards to appear and the discharging capacity can be further increased up to 894 mAh g<sup>-1</sup> (the blue lines in Figure 2a).

Another process, termed as Process A2, consisted of two steps. The first step was performed at room temperature using a pulse charging-discharging method which follows a square voltage waveform (Figure S4 in supplementary materials). This pulse charging-discharging method increases the capacitance significantly after 300 cycles, due to pre-fluorination of CNTA paper cathodes, as discussed in Figure S4. The second step was performed at 70°C following procedures similar to those described for Process A1 (Figure 2b). However, in the first induction cycle of Step 2 (the green lines in Figure 2b), the slope of the charging curve decreases and the potential plateau for the induced fluorination appears at a lower voltage, 4.47 V, when compared with those in Process A1. After applying three induction cycles with three controlled charging capacities (1400 mAh g<sup>-1</sup>, 2000 mAh g<sup>-1</sup>, and 2700 mAh g<sup>-1</sup>, respectively), the discharging capacity at 70°C was increased up to 2174 mAh g<sup>-1</sup> (the red lines in Figure 2b). It is important to note that, the discharging capacity did not increase if the induction charging capacities were further extended or if more induction cycles were added. Therefore, 2 induction cycles for Process A1 and 3 cycles for Process A2 are optimal. After the induction processes, the potential plateau for the induced fluorination disappeared below 4.5 V (will be seen in Figure 4). It indicates that certain reversible reactions were activated and optimized in the batteries. The batteries were then cycled at different rates within the voltage window between 1.4 V and 4.5 V to determine their performance at both 70°C and 22°C.

**Reversible fluorination of CNTA paper cathodes.** In an attempt to investigate the reversible reactions occurring at CNTA papers, the

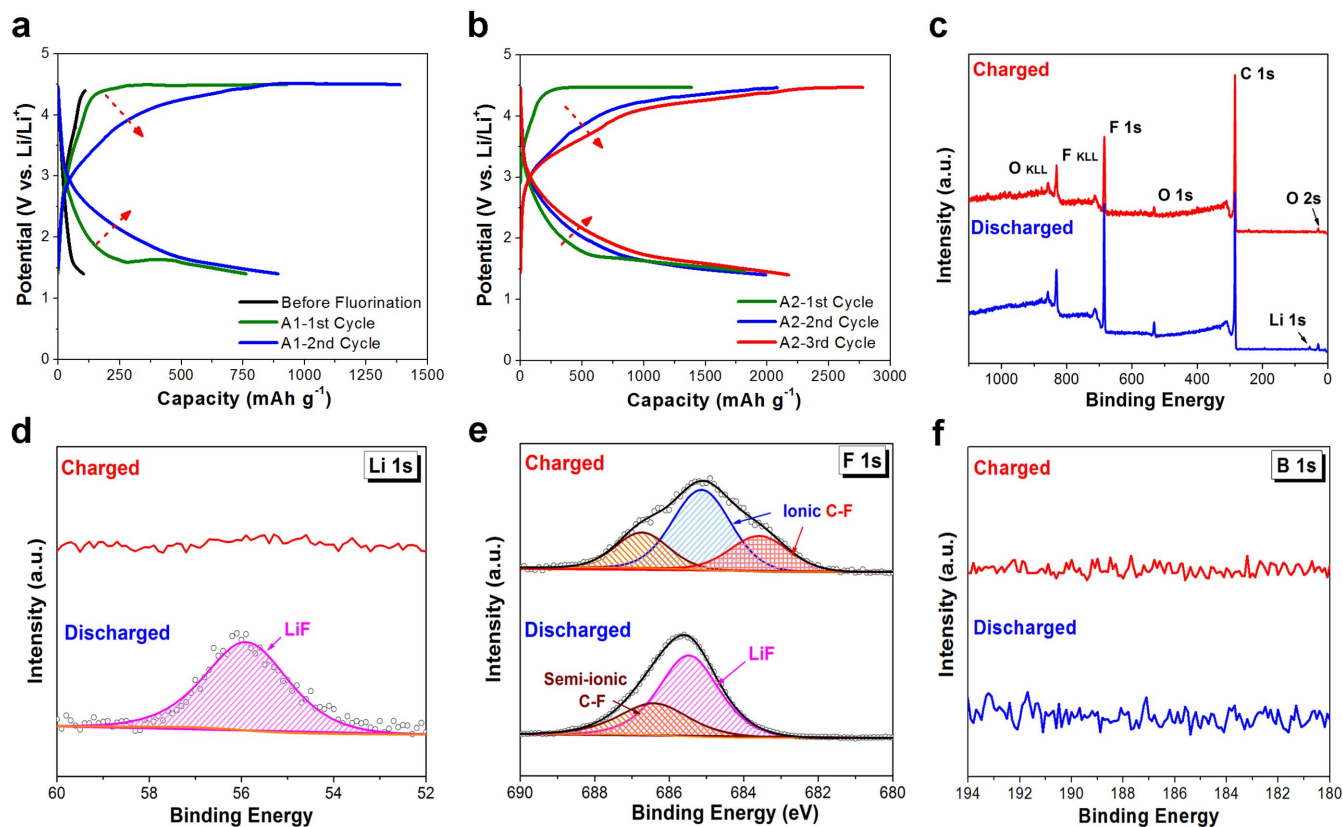
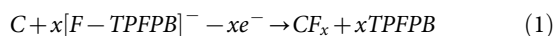


**Figure 2 | Induction processes and XPS characterization of the electrode materials.** (a) Process A1, two induction cycles at 70°C for the induced fluorination of CNTA papers. (b) Process A2, three induction cycles at 70°C after pulse-cycling treatment at room temperature. (c–f) XPS spectra of the charged and discharged samples; a.u., arbitrary units.

cells were disassembled and the active materials were characterized after they were charged to 4.5 V or discharged to 1.4 V, respectively. TPFPB was used in this study as a fluoride-anion receptor to dissolve LiF salts by displacing lithium cations from fluoride anions and forming  $[F\text{-TPFPB}]^-$  complex anions<sup>16</sup>.  $[F\text{-TPFPB}]^-$  is, therefore, the only source of fluorine in the current system. X-ray photoelectron spectroscopy (XPS) spectra in Figure 2c show high fluorine concentration in the charged sample. However, boron, a characteristic element of TPFPB, was not detected in the charged sample (Figures 2c and 2f). It indicates that CNTA papers have been fluorinated by the free fluoride ions released from  $[F\text{-TPFPB}]^-$ , and the intercalation of bulky  $[F\text{-TPFPB}]^-$  anions into the carbon cathode was suppressed. The free fluoride ions released from  $[F\text{-TPFPB}]^-$  are originally from the dissolved LiF salts, rather than from the decomposition of TPFPB molecules, which will be discussed later in this report. The same result was also observed for the sample charged to the end of the charging potential plateau in the first induction cycle. Therefore, the following reaction,

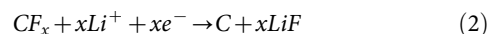


was occurring at the CNTA papers (Figure 1a), for the induced fluorination during the induction and/or for the charging after the induction.

Elemental mapping of carbon, fluorine and oxygen on the charged cathode was also performed by energy-filtering TEM (EFTEM) (Figure 3a). The distributions of carbon and fluorine are homogeneous and their concentration profiles completely overlap, suggesting the fluorination of CNTA papers, which agrees well with the XPS results. The bright-field transmission electron microscopy (TEM) image in Figure 3a shows the morphology of the fluorinated CNTA paper cathode. The tubular structure of most CNTs was destroyed, and the defective nanostructures were

formed surrounding the remaining CNTs that act as the electron conductive network for the reversible reactions. It is suggested that, during induced fluorination, fluoride ions were inserted into the CNT wall layers through the open ends of the CNTs and/or through the defects along the tubes, causing breakdown of the tubular structures (also see Figure S5 in supplementary materials). The destruction of the graphitic carbon structure may explain the disappearance of the charging potential plateau after the induced fluorination. The detailed analyses are in the discussion section. Figure 2e reveals that the inserted fluoride ions form ionic or semi-ionic C-F bonds<sup>19</sup> with the pure carbon cathodes, which also supports that TPFPB has not been decomposed at high voltages.

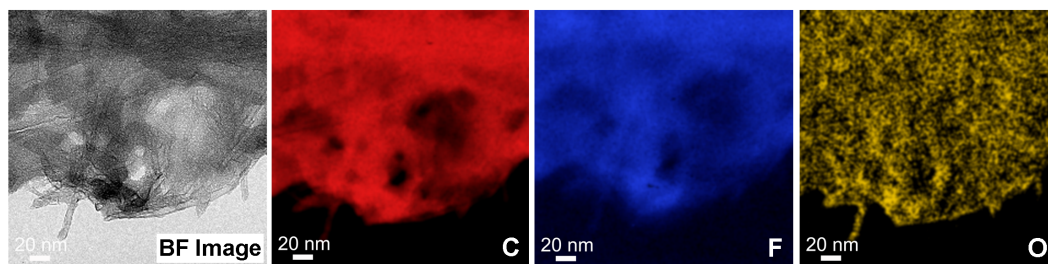
In the discharged sample, the high concentration of fluorine was also detected by XPS (Figure 2c), which is caused by the formation of lithium fluoride solids (Li: 56.0 eV and F: 685.0 eV)<sup>20</sup>, as indicated in Figure 2d. Therefore, during discharging, the in-situ formed carbon fluorides from Reaction (1) will be defluorinated by lithium cations transported from the anode, following the conversion reaction (Figure 1b):



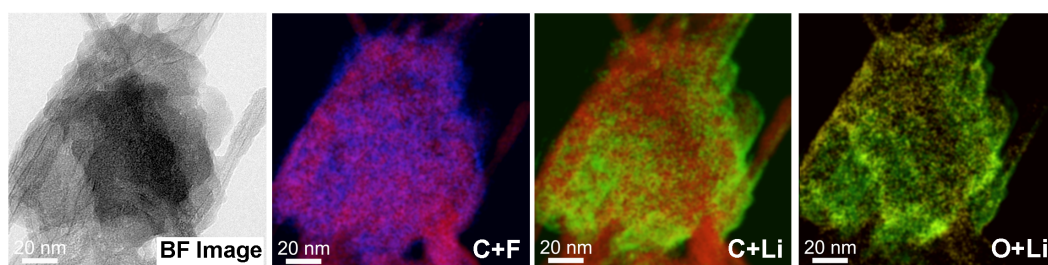
Elemental mapping of carbon, fluorine, lithium and oxygen on the discharged sample further proves the occurrence of Reaction (2) (Figure 3b). The elemental map of C + F in Figure 3b shows that the fluoride anions (blue) were excluded from the defective carbon matrix (red), and were bonded with lithium cations (green) forming LiF particles wrapping the carbon matrix (red) (the C + Li mapping image in Figure 3b). It is noted that, after the release of  $F^-$  ions, the carbon matrix maintains its defective structures, as shown in the TEM image in Figure 3b (also seen in XPS results in Figure S6 in supplementary materials).



### a. Charged



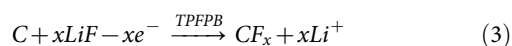
### b. Discharged



Lithium ( ■ ); Carbon ( ■ ); Fluorine ( ■ ); Oxygen ( ■ )

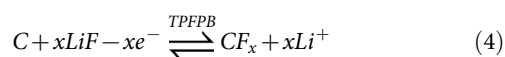
**Figure 3 | Morphology and phase distribution in the cathodes after fluorination and defluorination processes.** (a) Bright field (BF) TEM image showing the morphology and structure of the charged sample, followed by the false-color elemental maps of C (red), F (blue) and O (orange) obtained by energy-filtering imaging from the same region. (b) BF TEM image showing the morphology and structure of the discharged sample, followed by the false-color elemental maps of C (red) + F (blue), C (red) + Li (green), O (orange) + Li (green) obtained by energy-filtering imaging from the same region.

In the presence of TFPFB, LiF solids formed during discharging are a metastable phase in the current system. Interestingly, no LiF solids were detected by XPS in the charged sample (Figure 2d). The same result was also obtained from Li K-edge electron energy-loss spectroscopy (EELS) spectra (Figure S7 in supplementary materials). It indicates that, with assistance of TFPFB, the metastable LiF solids formed in Reaction (2) during discharging will be dissociated in the next charging step by their reaction with the defective carbons (Figure 1c):



It is believed that the presence of TFPFB, the reaction temperature, and the defective carbons are three important factors for the occurrence of the reversed conversion reaction (Reaction (3)). During charging, Reaction (1) and Reaction (3) are competitive. Although Reaction (1) is more favorable than Reaction (3), metastable LiF solids wrapping around the carbon matrix (the C + Li mapping image in Figure 3b) may block the accessibility of [F-TFPFB]<sup>-</sup> complex anions to the defective carbons and retard Reaction (1). Therefore, it is suggested that Reaction (1) mainly occurred at the induced-fluorination potential plateau over 4.4 V during induction, and Reaction (3) mainly occurred during charging after the induction processes.

In general, the reversible fluorination/defluorination reactions occurring at CNTA papers activated by the induced fluorination can be written as:



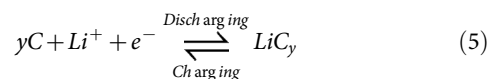
Meanwhile, the induced fluorination caused the destruction of the tubular CNT structures to the defective nanostructures.

The low concentration of oxygen in both the charged and discharged samples (Figure 2c) implies that the decomposition of the organic electrolyte was restricted to a low level. The O + Li image in Figure 2e suggests that oxygen is bonded to the carbon matrix, rather

than to the lithium to form lithium oxides, e.g., Li<sub>2</sub>O<sub>2</sub>, as in Li-air batteries.

**Lithium-ion storage by defective carbon.** A high discharging capacity of 2174 mAh g<sub>carbon</sub><sup>-1</sup> was obtained in Figure 2b. If it were solely contributed from Reaction (2), Reaction (2) would deplete [F-TFPFB]<sup>-</sup> complex anions in the electrolyte and cause problems to the performance in the following cycles. However, Figure 4 shows excellent battery performance in terms of energy density and cyclability for Li-CNT-F batteries. It indicates that another storage mechanism co-exists in the current system. The C + Li mapping image in Figure 3b shows some overlapped region between C and Li (yellow color in C + Li), suggesting the lithium-ion storage in the defective carbon structures.

Traditional intercalation-type graphite materials in LIB can deliver a lithium-ion storage capacity of 372 mAh/g by forming LiC<sub>6</sub> at the potential of 0 ~ 0.2 V. However, some disordered carbons<sup>24</sup> were shown to have a capacity much higher than 372 mAh g<sup>-1</sup>, and demonstrated reasonable capacities over 1.0 V<sup>22-26</sup>. The storage of lithium ions by carbon defective structures, such as functional groups<sup>22,23</sup>, increased interlayer spacing<sup>24,27</sup>, and edges and vacancies<sup>26,28</sup>, were rationalized. Hence, the defective carbons resulted from the induced fluorination are also suggested to storage lithium ions in this lithium-carbon configuration (Figures 1b and 1c).



**Electrochemical testing of Li-CNT-F batteries.** According to the discussion above, Li-CNT-F batteries exhibit a dual-storage mechanism, reversible fluorination/defluorination (Reaction (4)) and lithium-ion storage/release (Reaction (5)), occurring at the carbon cathodes, which was activated by the induced fluorination of CNTA papers. Excellent battery performance in terms of energy density and

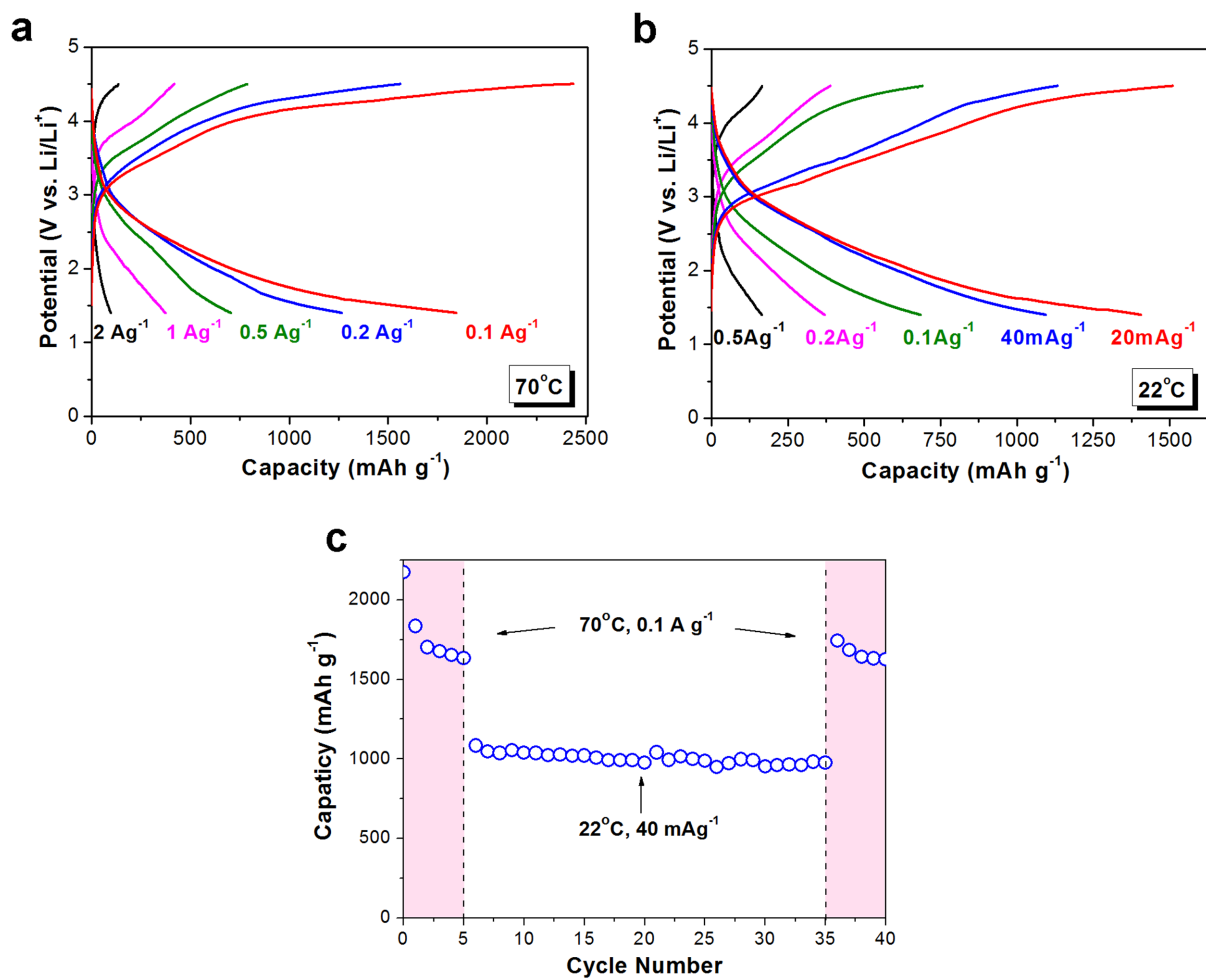


**Figure 4** | Performance of Li-CNT-F batteries after Process A2. Charge-discharge curves at different rates at 70°C (a) and at 22°C (b) after Process A2. (c) Cycle life test performed under different conditions, 0.1 A g<sup>-1</sup> at 70°C and 40 mA g<sup>-1</sup> at 22°C, on the same battery for up to 40 cycles in total.

cyclability was obtained for Li-CNT-F batteries due to the dual-storage mechanism. A maximum discharging capacity of 2174 mAh g<sub>carbon</sub><sup>-1</sup> and an energy density of 4113 Wh kg<sub>carbon</sub><sup>-1</sup> were achieved during the third induction cycle at 70°C in Process A2 (the red lines in Figure 2b). To the best of our knowledge, these results are 5 times higher than the best capacities previously reported for the lithium-carbon battery configuration<sup>21–23,26</sup>. Figure 4 shows the performance of Li-CNT-F batteries after induction Process A2. The reversible reactions demonstrate higher kinetics (higher power density) at 70°C (Figure 4a) than that at 22°C (Figure 4b). Interestingly, at 22°C, the discharging capacity also maintains a high level, 1406 mAh g<sub>carbon</sub><sup>-1</sup>, corresponding to an energy density of 2982 Wh kg<sub>carbon</sub><sup>-1</sup>, with a coulombic efficiency (~97%) (Figures 4b) higher than that at 70°C (~76%) (Figure 4a). Figure 4c shows that the discharging capacity decreases slowly from 2174 mAh g<sub>carbon</sub><sup>-1</sup> to 1640 mAh g<sub>carbon</sub><sup>-1</sup> in the initial 5 cycles when cycling at 70°C with a current density of 0.1 A g<sup>-1</sup>. Further cycling at 22°C with a current density of 40 mA g<sup>-1</sup>, the battery shows high reversible capacity at ~1000 mAh g<sub>carbon</sub><sup>-1</sup>, with the capacity retention being 93% after 30 cycles. When cycling the battery back at 70°C, the original capacity was largely recovered to ~1640 mAh g<sub>carbon</sub><sup>-1</sup>, demonstrating good cycling performance.

Figure 5 compares the performance of different batteries on the Ragone plot normalized to the weight of cathode materials, i.e., carbon for Li-CNT-F batteries, sulfur for Li-S and carbon + oxygen for Li-O<sub>2</sub> batteries. At 22°C, Li-CNT-F batteries outperform other types of lithium-carbon-configuration batteries, including previously reported Li-functionalized CNT<sup>22</sup> and Li-reduced graphene oxide

batteries<sup>23</sup> using carboxyl groups for lithium-ion storage. Their performance is also higher than Li-S batteries and close to that of Li-O<sub>2</sub> batteries. However, for the data presented as Li-S batteries<sup>2–7</sup>, the cathodes only contain 30 wt.% to 60 wt.% of sulfur, over half of the cathode is not active materials. For those results presented as Li-O<sub>2</sub> batteries<sup>8–11</sup>, the energy densities reduce by half after 10 cycles. Therefore, CNTA paper cathodes with no binding materials and no conductive additives show remarkable features in Figure 5. More importantly, the performance of Li-CNT-F batteries will also increase appreciably with increasing temperatures (indicated by a red curve in Figure 5), demonstrating their great potential to be the future energy storage systems.

The mass of the battery includes the mass of the anode, electrolyte, and other inert components in the battery. A reduction factor, mass of the battery/mass of the cathode, is normally used to estimate the battery performance from the cathode performance. For conventional LIBs, the reduction factor is in the range between 2.5 and 3 depending on the type of lithium-transition metal oxide cathodes<sup>1,22,29</sup>. The reduction factor for Li-S is claimed to be in the range of 4 to 7<sup>1</sup>, and that for Li-O<sub>2</sub> batteries is still unknown. For Li-CNT-F batteries, the fluoride ions in the electrolyte were involved in activating the dual-storage mechanism, and therefore, a large reduction factor of 10 was used to conservatively estimate their battery performance, which is ~300 Wh kg<sub>battery</sub><sup>-1</sup> at 22°C.

## Discussion

The complex anion of [F-TPFPB]<sup>-</sup> was previously found to be reversibly intercalated in graphite with limited capacity<sup>16</sup>, 60 ~

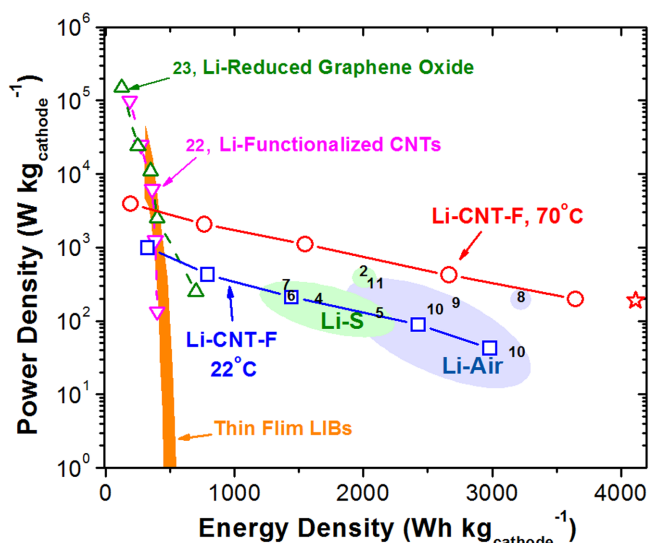


**Figure 5** | Ragone plot, comparing Li-CNT-F batteries with other batteries in terms of weight of cathode materials. The highest energy density for Li-CNT-F batteries, 4113 Wh kg<sub>carbon</sub><sup>-1</sup>, obtained during the third 70°C-induction cycle in Process A2, is presented as a red star.

80 mA g<sub>carbon</sub><sup>-1</sup>. It is the intercalation of the bulky complex anion of [F-TPFPB]<sup>-</sup> that will sterically hinder further anion intercalation and worsen the cathode specific capacity<sup>16</sup>. However, in this report, the intercalation of [F-TPFPB]<sup>-</sup> was successfully suppressed, as suggested in Figure 2f, which may explain the high capacity achieved in Figure 4. The suppression of bulky [F-TPFPB]<sup>-</sup> intercalation is due to the particular induction temperature (70°C) conducted, which reduces the energy barrier for the F<sup>-</sup> release from [F-TPFPB]<sup>-</sup>, and therefore, promotes the intercalation of free F<sup>-</sup> in CNTA papers. It is also worth to note that the free fluoride ions released from [F-TPFPB]<sup>-</sup> are originally from the dissolved LiF salts, rather than from the decomposition of TPFPB molecules. It has been calculated that the energy barrier for the fluoride anion release from TPFPB (59.2 kcal/mol) is much lower than the breakdown of a true covalent bond (typically on the order of 100 kcal/mol) in TPFPB<sup>16</sup>.

As indicated by the red arrows in Figures 2a and 2b, the polarization between charge and discharge curves was decreasing with increasing induction cycles, revealing that the energy barriers for the reversible reactions were reducing with induction cycles at the same induction temperature of 70°C. It implies that both Reaction (4) and Reaction (5) were facilitated at 70°C after the induced fluorination, which is attributed to the defective carbon structures.

The temperature factor to reduce the energy barrier for the F<sup>-</sup> release from [F-TPFPB]<sup>-</sup> vanishes when running the batteries at 22°C. However, the discharging capacity at 22°C was also significantly improved after the induction processes (Figure S9 in supplementary materials). This result further suggests that the in-situ formed defective carbon structure plays an important role in facilitating both Reaction (4) and Reaction (5).

It is, therefore, concluded that: 1) the presence of TPFPB and the induction temperature of 70°C are two main reasons for the induced fluorination of CNTA paper cathodes; 2) the induced fluorination activates the reversible reactions of Reaction (4) and Reaction (5), and destructs the graphitic carbon to defective nanostructures; 3) the in-situ formed defective carbons, further, facilitate the reversible reactions at both 70°C and 22°C.

According to XPS results in Figure 2, the atomic ratio between carbon and fluorine is calculated to be 4:1, and hence, it is the formation of CF<sub>0.2</sub> during charging for the sample after Induction Process A1. The capacity contribution from the fluorination during charging is then calculated to be 447 mAh g<sup>-1</sup>. Therefore, the

respective capacity contribution from the two storage mechanisms is determined to be around 1:1.

The relatively large polarization between charge and discharge is still present in Figures 4a and 4b, which penalizes the energy efficiency, 40–60%, for the current Li-CNT-F battery systems, although similar challenge exists in many other battery systems<sup>30</sup> such as Li-air (40–70%)<sup>8–11</sup> and Zn-air batteries (40–70%)<sup>31,32</sup>. The polarization is suggested to be related to the energy barrier to dissociate LiF metastable solids. The relatively low power density at 22°C should be attributed to the sluggish kinetics for the reversible fluorination/defluorination reactions at room temperature and the defective carbon structures formed during the induction processes. The development of an efficient catalyst to reduce the polarization and increase the power density at room temperature requires further investigations in the future. Furthermore, the polarization, the power density and the cyclability are also dependent on the degree of induction (activation), which should be considered as an important parameter when making Li-C-F batteries for various applications. This work may also point out the potential of using cheap defective carbons as the cathode for the next generation rechargeable batteries.

In conclusion, we realized the induced fluorination of CNTA paper cathodes by an in-situ electrochemical induction process at 70°C and in the presence of TPFPB. The induced fluorination of CNTA papers activated the reversible fluorination/defluorination reactions and lithium-ion storage/release at the CNTA paper cathodes, resulting in a dual-storage mechanism. It is the first time that the reversible fluorination/defluorination reactions were realized at pure carbon and non-fluoride materials. In addition, the induced fluorination destructed the graphitic carbon to defective nanostructures, which further facilitated the two reversible reactions at both 70°C and 22°C. The rechargeable battery with this dual-storage mechanism demonstrated a maximum discharging capacity of 2174 mAh g<sub>carbon</sub><sup>-1</sup> and a specific energy of 4113 Wh kg<sub>carbon</sub><sup>-1</sup> with good cycling performance. This paper uncovers the significance of energy storage by carbon materials at high voltages, and demonstrates the Li-C-F battery system a new promising candidate for the future energy storage systems.

## Methods

**Battery fabrication and testing.** Millimeter-thick multi-walled CNT arrays were grown on the whole 4- or 6-inch silicon wafers, following water-assisted chemical vapor deposition (WACVD) method reported elsewhere<sup>18</sup>. The as-grown 1.2 ± 0.2 mm-thick CNT arrays on the silicon wafers were rolled and pressed to CNT array (CNTA) papers. After peeling from the wafer, each CNTA paper was measured to be 35 ± 3 μm thick using a micrometer screw-gauge and can be cut into the size of the electrodes for making pouch cells. Two pieces of CNTA papers were stacked together to make one single cathode with a thickness of 70 ± 6 μm and a CNT mass loading of 1.4–1.8 mg cm<sup>-2</sup>. After drying at 120°C overnight in a vacuum oven, these conductive and binder-free CNTA papers were cut into 1 cm<sup>2</sup> electrodes and assembled into 2032-type coin cells in a glove box, using a piece of Li metal as the anode, two sheets of microporous membrane (Celgard 2500, Celgard) as the separator, and 200 μl of 0.8 M LiF and 0.8 M tris(pentafluorophenyl)borane (TPFPB) in ethylene carbonate (EC)/dimethyl carbonate (DMC) (1:2, v/v) as the electrolyte.

Galvanostatic charge/discharge tests, cyclic voltammetry (CV) tests and cycle performance tests were conducted at 22 ± 1°C and/or 70 ± 1°C using a 1470E multi potentiostat/celltest system (Solartron). The induced fluorination of CNTA paper cathodes was realized electrochemically during two induction processes, Process A1 and Process A2. Both processes contained a controlled charging capacity step, which was performed at 70°C and a current density of 0.1 A g<sup>-1</sup> with different controlled charging capacities. An additional step, the pulse charging-discharging step, was added to Process A2 before the controlled charging capacity step. This step was performed at 22°C, during which the as-assembled cells were pulse-charged to 4.5 V, held for 10 min, pulse-discharged to 1.5 V and then held for 5 min, following a square voltage waveform, for many cycles (Figure S4). The pulse charging and discharging rates were controlled to be the same and were at three different levels: 10 A g<sup>-1</sup>, 20 A g<sup>-1</sup> and 50 A g<sup>-1</sup>. The rate was increased by one level after every 100 cycles up to a total of 300 cycles. Cyclic voltammetry tests in the range between 1.5 V and 4.5 V were conducted for the evaluation of the performance for every 50 cycles.

**Characterization.** CNTA paper cathodes were characterized both in the charged (fluorinated) and discharged (defluorinated) states using samples from the same paper cathode. After the Li-CNT-F was charged to 4.5 V, the battery cell was disassembled to obtain the CNTA paper cathode. This cathode was cut into two after



being thoroughly rinsed with DMC and kept in a vacuum in the glove box. One half of the cathode was kept for characterization as the charged sample; the other half was reassembled in the 2032-type coin cell, and discharged to 1.4 V before being removed from the battery and characterized as the discharged sample. In order to minimize the exposure of the cathode materials to the air, all the samples used for TEM and X-ray photoelectron spectroscopy (XPS) were prepared inside the glove box and transferred to the examining stages using an argon protected sample loading holder.

The morphology and structure of CNTAs were analyzed by scanning electron microscopy (SEM, Hitachi S-4800, operated at 10 kV and 20 kV). Transmission electron microscopy (TEM, JEOL JEM-2100 with LaB<sub>6</sub> cathode, 200 kV) was used to characterize the structural changes of CNTA paper electrodes before and after fluorination. XPS was carried out using a Kratos AXIS Ultra-x-ray photoelectron spectrometer. Energy-filtering TEM (EFTEM) was employed for elemental mapping calculations. Mapping was performed on a H-9500 TEM equipped with a Gatan Imaging Filter (GIF) spectrometer. In order to decrease possible electron beam damage to the sample, an accelerating voltage of 100 kV was employed. All energy-filtering images were recorded using a binning of  $2 \times 2$  giving  $1024 \times 1024$  pixel images, for reasons of sensitivity. Because the focus of an EFTEM image differs significantly from the focus of the elastic image, the images were focused at an energy-loss between 100 and 200 eV. The three-window method which is effective at reducing thickness effects was used for elemental mapping. Electron energy-loss spectroscopy (EELS) spectra were collected in image mode with an energy resolution of  $\sim 1.3$  eV as measured by the full width at half maximum (FWHM) of the zero-loss peak (ZLP).

- Bruce, P. G., Freunberger, S. A., Hardwick, L. J. & Tarascon, J. M. Li-O<sub>2</sub> and Li-S batteries with high energy storage. *Nat. Mater.* **11**, 19–29 (2012).
- Seh, Z. W. *et al.* Sulphur-TiO<sub>2</sub> yolk-shell nanoarchitecture with internal void space for long-cycle lithium-sulphur batteries. *Nat. Commun.* **4**, 133 (2013).
- Wang, H. *et al.* Graphene-wrapped sulfur particles as a rechargeable lithium-sulfur battery cathode material with high capacity and cycling stability. *Nano Lett.* **11**, 2644–2647 (2011).
- Xin, S. *et al.* Smaller sulfur molecules promise better lithium-sulfur batteries. *J. Am. Chem. Soc.* **134**, 18510–18513 (2012).
- Ji, X., Lee, K. T. & Nazar, F. A highly ordered nanostructured carbon-sulphur cathode for lithium-sulphur batteries. *Nat. Mater.* **8**, 500–506 (2009).
- He, M., Yuan, L. X., Zhang, W. X., Hu, X. L. & Huang, Y. H. Enhanced cyclability for sulfur cathode achieved by a water-soluble binder. *J. Phys. Chem. C.* **115**, 15703–15709 (2011).
- Ji, X., Ever, S., Black, R. & Nazar, F. Stabilizing lithium-sulphur cathodes using polysulphide reservoirs. *Nat. Commun.* **2**, 325 (2011).
- Jung, H. G., Hassoun, J., Park, J. B., Sun, Y. K. & Scrosati, B. An improved high-performance lithium-air battery. *Nat. Chem.* **4**, 579–585 (2012).
- Qin, Y. *et al.* In situ fabrication of porous-carbon-supported  $\alpha$ -MnO<sub>2</sub> nanorods at room temperature: application for rechargeable Li-O<sub>2</sub> batteries. *Energy Environ. Sci.* **6**, 519–531 (2013).
- Mitchell, R. R., Gallant, B. M., Thompson, C. V. & Horn, Y. S. All-carbon-nanofiber electrodes for high-energy rechargeable Li-O<sub>2</sub> batteries. *Energy Environ. Sci.* **4**, 2952–2958 (2011).
- Christensen, J. *et al.* A critical review of Li/air batteries. *J. Electrochem. Soc.* **159**, R1–R30 (2012).
- Fulvio, P. F. *et al.* Low-temperature fluorination of soft-templated mesoporous carbons for a high-power lithium/carbon fluoride battery. *Chem. Mater.* **23**, 4420–4427 (2011).
- Chamssedine, F. *et al.* Reactivity of carbon nanofibers with fluorine gas. *Chem. Mater.* **19**, 161–172 (2007).
- Guérin, K. *et al.* Synthesis and characterization of highly fluorinated graphite containing sp<sup>2</sup> and sp<sup>3</sup> carbon. *Chem. Mater.* **16**, 1786–1792 (2004).
- Mickelson, E. T. *et al.* Fluorination of single-walled carbon nanotubes. *Chem. Phys. Lett.* **296**, 188–194 (1998).
- West, W. C. *et al.* Reversible intercalation of fluoride-anion receptor complexes in graphite. *J. Electrochem. Soc.* **154**, A929–A936 (2007).
- Yazami, R. *et al.* Fluorinated carbon nanofibres for high energy and high power densities primary lithium batteries. *Electrochem. Commun.* **9**, 1850–1855 (2007).
- Cui, X., Wei, W. & Chen, W. Lengthening and thickening of multi-walled carbon nanotube arrays grown by chemical vapor deposition in the presence and absence of water. *Carbon* **48**, 2782–2791 (2010).
- Palchan, I., Crespín, M., Estrade-Szwarczkopf, H. & Rousseau, B. Graphite fluorides: an XPS study of a new type of C-F bonding. *Chem. Phys. Lett.* **157**, 321–327 (1989).
- Kim, B. G., Lee, J. N., Lee, D. J., Park, J. K. & Choi, J. W. Robust cycling of Li-O<sub>2</sub> batteries through the synergistic effect of blended electrolytes. *Energy Environ. Sci.* **6**, 443–448 (2013).
- Stoller, M. D. *et al.* Activated graphene as a cathode material for Li-ion hybrid supercapacitors. *Phys. Chem. Chem. Phys.* **14**, 3388–3391 (2012).
- Lee, S. W. *et al.* High-power lithium batteries from functionalized carbon-nanotube electrodes. *Nat. Nanotechnol.* **5**, 531–537 (2010).
- Jang, B. Z. *et al.* Graphene surface-enabled lithium ion-exchanging cells: next-generation high-power energy storage devices. *Nano Lett.* **11**, 3785–3791 (2011).
- Sato, K., Noguchi, M., Demachi, A., Oki, N. & Endo, M. A mechanism of lithium storage in disordered carbons. *Science* **264**, 556–558 (1994).
- Wu, Y. P., Wan, C. R., Jiang, C. Y., Fang, S. B. & Jiang, Y. Y. Mechanism of lithium storage in low temperature carbon. *Carbon* **37**, 1901–1908 (1999).
- Zhamu, A. *et al.* Reviving rechargeable lithium metal batteries: enabling next-generation high-energy and high-power cells. *Energy Environ. Sci.* **5**, 5701–5707 (2012).
- Suzuki, T., Hasegawa, T., Mukai, S. R. & Tamon, H. A theoretical study on storage states of Li ions in carbon anodes of Li ion batteries using molecular orbital calculations. *Carbon* **41**, 1933–1939 (2003).
- Dahn, J. R., Zheng, T., Liu, Y. & Xue, J. S. Mechanisms for lithium insertion in carbonaceous materials. *Science* **270**, 590–593 (1995).
- Wang, X., Hou, Y., Zhu, Y., Wu, Y. & Holze, R. An aqueous rechargeable lithium battery using coated Li metal as anode. *Sci. Rep.* **3**, 1401 (2013).
- Thakur, M., Sinsabaugh, S., Isaacson, M. J., Wong, M. S. & Biswal, S. L. Inexpensive method for producing macroporous silicon particulates (MPSPs) with pyrolyzed polyacrylonitrile for lithium ion batteries. *Sci. Rep.* **2**, 795 (2012).
- Li, Y. *et al.* Advanced zinc-air batteries based on high-performance hybrid electrocatalysts. *Nat. Commun.* **4**, 1805 (2013).
- Toussaint, G., Stevens, P., Akrou, L., Rouget, R. & Fourgeot, F. Development of a rechargeable zinc-air battery. *ECS Trans.* **28**, 25–34 (2010).

## Acknowledgments

The authors would like to thank Alberta Innovates-Energy and Environment Solutions (AIEES) and NanoBridge for financial support. The authors are grateful to Dr. Mark Summers for his many valuable suggestions in shaping the project to the current stage, and Drs. Surinder Singh, John Zhou, Mr. Rick Nelson and Dr. Eddy Isaacs for making the project happen. The authors would also like to acknowledge Drs. Xiao-Qing Yang and Hung-Sui Lee, Brookhaven National Laboratory, Upton, USA, for supplying a high purity chemical reagent for comparative studies, and Drs. Douglas Ivey and Thomas Thundat, University of Alberta, for proof reading the manuscript.

## Author contributions

X.W.C. conceived and designed the experiments. X.W.C. did most part of the work with assistance from T.F.W. J.C. performed the energy filtering TEM imaging characterization. W.X.C. co-conceived the concept and provided supervision during the entire course of the investigation.

## Additional information

**Supplementary information** accompanies this paper at <http://www.nature.com/scientificreports>

**Competing financial interests:** The authors declare no competing financial interests.

**How to cite this article:** Cui, X., Chen, J., Wang, T. & Chen, W. Rechargeable Batteries with High Energy Storage Activated by In-situ Induced Fluorination of Carbon Nanotube Cathode. *Sci. Rep.* **4**, 5310; DOI:10.1038/srep05310 (2014).



This work is licensed under a Creative Commons Attribution-NonCommercial-NoDerivs 4.0 International License. The images or other third party material in this article are included in the article's Creative Commons license, unless indicated otherwise in the credit line; if the material is not included under the Creative Commons license, users will need to obtain permission from the license holder in order to reproduce the material. To view a copy of this license, visit <http://creativecommons.org/licenses/by-nc-nd/4.0/>